



HAL
open science

Terahertz photo-generated current in a two-dimensional quantum dot system

R. Rodrigues Oliveira, D. da Costa, G. Farias, R. Ferreira, A. Chaves

► **To cite this version:**

R. Rodrigues Oliveira, D. da Costa, G. Farias, R. Ferreira, A. Chaves. Terahertz photo-generated current in a two-dimensional quantum dot system. *Journal of Applied Physics*, 2020, 128 (18), pp.185702. 10.1063/5.0025181 . hal-03095509

HAL Id: hal-03095509

<https://hal.science/hal-03095509v1>



Submitted on 16 Sep 2024

HAL is a multi-disciplinary open access archive for the deposit and dissemination of scientific research documents, whether they are published or not. The documents may come from teaching and research institutions in France or abroad, or from public or private research centers.

L'archive ouverte pluridisciplinaire **HAL**, est destinée au dépôt et à la diffusion de documents scientifiques de niveau recherche, publiés ou non, émanant des établissements d'enseignement et de recherche français ou étrangers, des laboratoires publics ou privés.

RESEARCH ARTICLE | NOVEMBER 11 2020

Terahertz photo-generated current in a two-dimensional quantum dot system

R. Rodrigues Oliveira; D. R. da Costa; G. A. Farias; R. Ferreira; A. Chaves  

 Check for updates

J. Appl. Phys. 128, 185702 (2020)

<https://doi.org/10.1063/5.0025181>





Instruments for Advanced Science

- Knowledge
- Experience
- Expertise

Click to view our product catalogue

Contact Hiden Analytical for further details:
www.HidenAnalytical.com
info@hiden.co.uk

Gas Analysis	Surface Science	Plasma Diagnostics	Vacuum Analysis
<ul style="list-style-type: none">dynamic measurement of reaction gas streamscatalysis and thermal analysismolecular beam studiesdissolved species probesfermentation, environmental and ecological studies	<ul style="list-style-type: none">UHV TPDSIMSend point detection in ion beam etchelemental imaging - surface mapping	<ul style="list-style-type: none">plasma source characterizationetch and deposition process reaction kinetic studiesanalysis of neutral and radical species	<ul style="list-style-type: none">partial pressure measurement and control of process gasesreactive sputter process controlvacuum diagnosticsvacuum coating process monitoring


Terahertz photo-generated current in a two-dimensional quantum dot system

Cite as: J. Appl. Phys. 128, 185702 (2020); doi: 10.1063/5.0025181

Submitted: 13 August 2020 · Accepted: 26 October 2020 ·

Published Online: 11 November 2020



R. Rodrigues Oliveira,^{1,a)} D. R. da Costa,^{1,2} G. A. Farias,¹ R. Ferreira,³ and A. Chaves^{1,b)} 

AFFILIATIONS

¹Departamento de Física, Universidade Federal do Ceará, Caixa Postal 6030, 60455-760 Fortaleza, Ceará, Brazil

²Department of Electrical and Computer Engineering, University of Minnesota, 200 Union Street SE, 4-174 Keller Hall, Minneapolis, Minnesota 55455-0170, USA

³Laboratoire de Physique de l'Ecole Normale Supérieure, ENS, Université PSL, CNRS, Sorbonne Université, Université de Paris, 75005 Paris, France

^{a)}Electronic mail: ravenna.rodrigues@fisica.ufc.br

^{b)}Author to whom correspondence should be addressed: andrey@fisica.ufc.br

ABSTRACT

The photo-generated current due to electronic transitions in a semiconductor planar quantum dot attached to outgoing leads is theoretically investigated. An electron is confined in the dot by a pure quantum mechanical effect, which is due to the higher ground state energy of the quantum wells forming the leads, as compared to the one in the dot. The dynamics of such a confined electron interacting with a light pulse is investigated by numerically solving a time-dependent Schrödinger equation within the effective mass approximation and goes beyond the lowest order perturbative approach. Our results show the coexistence of both linear and non-linear contributions to the photo-generated current in this system, sharply peaked at frequencies in the terahertz range, which are further tunable by the quantum dot radius. The peaks can be made even sharper as one adds a narrow constriction in the dot-leads connection. The details of the dependence of the peaks' frequency, intensity, and sharpness on system parameters are discussed.

Published under license by AIP Publishing. <https://doi.org/10.1063/5.0025181>

I. INTRODUCTION

Photodetectors are an important component of current electronics and are used in several fields such as telecommunications, astronomy, imaging devices, laser ranging, remote sensing, and others.^{1,2} Over the past few years, many photodetecting devices were developed, mostly based on semiconductor heterostructures.^{3,4} Many of these devices operate in infrared or mid-infrared frequencies,^{5,6} while photodetection in the terahertz (THz) frequency domain is still proven to be challenging. The pursuit for novel technological applications in THz has attracted increasing interest for many reasons, including its higher bandwidth, as compared to millimeter wave or microwave systems, and the fact that this frequency range has less interaction with the environment, since there is typically less ambient THz light noise as compared to infrared light noise.⁷ Infrared frequency is heavily employed in wireless devices, and as the number of devices grows, saturation in the advances on infrared based communications is highly anticipated, which has been

stimulating the development of novel technologies that go beyond this frequency range.⁷⁻⁹

An interesting example of an infrared photodetector was proposed in Ref. 6, where a semiconductor heterostructure forms a quantum well, defined in between two narrow and higher energy barriers, followed by longer lower energy barriers. This can be achieved by assuming, e.g., an alloy $\text{Ga}_x\text{Al}_{(1-x)}\text{As}$ as barrier and ALAs as a quantum well, so that a higher concentration x within finite regions near the ALAs well would provide the higher energy finite barriers. The quantum confinement potential is, thus, formed by the conduction band mismatch between the materials. For a confined electron in the ground state of the quantum well, in the absence of narrow barriers, any light frequency with energy higher than the difference between the barrier energy and the ground state energy would lead to a photo-generated current. However, in the presence of narrow higher energy barriers, a much better control of the photo-current is demonstrated: the current is peaked only at

16 September 2024, 10:10:07

the energies that match transition energies between the quantum well discrete states, with the peak's width being controlled by the height of the narrow barriers.

Many other examples of photodetectors based on semiconductor quantum dots have been proposed in the literature as well.^{10,11} For example, Su *et al.*¹² observed ≈ 4 THz photoresponse at temperatures up to 150 K in a photodetector based on $\text{In}_{0.6}\text{Al}_{0.4}\text{As}$ /GaAs self-assembled quantum dots. The THz absorption occurs due to inter-sublevel transitions in the discrete spectrum of the quantum dots. A similar idea has been employed in Ref. 13, which proposes a quantum dot-based photoresponse device whose operation frequencies can be tuned from 6.0 to ≈ 3.3 THz via an external gate voltage. More recently, inter-sublevel transitions have also been probed by THz spectroscopy in self-assembled InAs quantum dots in Ref. 14. Despite the existence of well-established quantum dot and quantum well-based photodetectors in the literature, it is interesting to propose alternative ways to provide photocurrent in low-dimensional devices, especially in the THz range. Different low-dimensional systems pose different challenges for fabrication and further applicability in novel technologies. In this sense, the study of photoresponse in low-dimensional systems based on planar quantum dots, created with two-dimensional electron gases or layered materials,^{15,16} is of current interest toward alternative venues to advance the field of opto-electronics.

In this paper, we investigate the interaction between light and electrons confined in a planar semiconductor quantum dot attached to co-linear leads. The energy spectrum of the dot-leads system has a discrete series of low-lying states confined in the QD (as the initially occupied ground one), followed by a higher energy continuum with a series of resonances displaying enhanced localization in the QD region but non-vanishing wings in the leads regions. Photodetector devices may take profit of such quasi-resonant states, which bridge the strongly quantized initial state and the final quasi-classical leads states. Indeed, we show here that they greatly affect the absorption spectrum of the QD (which would be otherwise broadband) by enhancing absorption in a narrow energy range. We additionally show that, in a properly designed system of a large QD with a few resonant states, the non-linear photoresponse at high excitations is also greatly enhanced, and that (in strike contrast to optical or near infrared devices) both linear and non-linear peaks share the same spectral range (around a few THz). To this end, the dynamics of the initially confined electron interacting with light and the possibility of obtaining photocurrent in this system are investigated by numerically solving the time-dependent Schrödinger equation within the effective mass approximation, which allows us exploring the non perturbative regime at high excitations.

II. THEORETICAL MODEL

The system proposed here is sketched in Fig. 1. It consists of a planar circular quantum dot of radius R attached to two co-linear leads of width d_2 . A constriction of width d_1 and length L is made in the vicinity of the quantum dot. The confinement potential is assumed to consist of a sharp barrier surrounding the whole system, while it is zero in the shaded region in Fig. 1. For numerical purposes, we take $V_0 = 600$ meV, which is in the order of

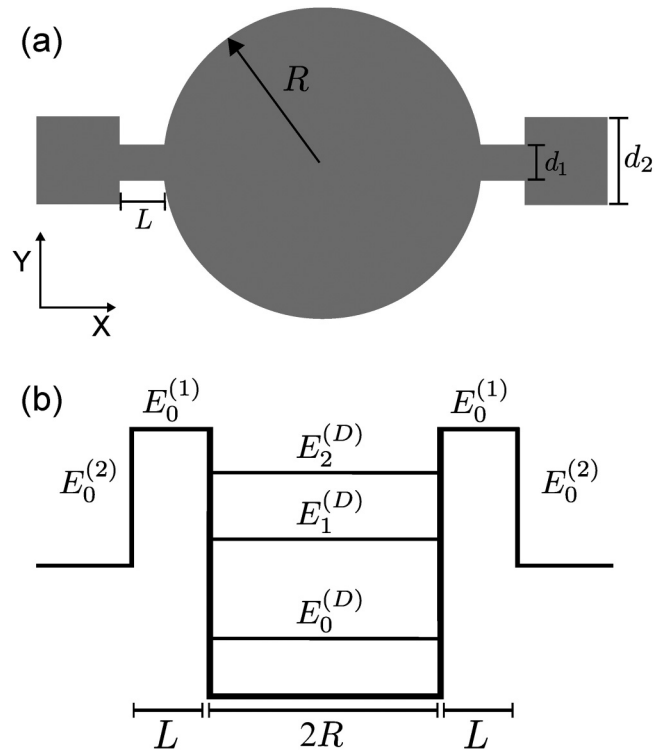


FIG. 1. (a) Sketch of the system, consisting of a circular quantum dot of radius R , attached to leads of width d_2 , which present a constriction of width d_1 and length L in the vicinity of the dot. (b) Energy landscape experienced by an electron traveling across this system in the absence of fields ($E_{st} = E_{dyn} = 0$). In the wide leads, the lowest electron energy is the ground state energy $E_0^{(2)}$ of the quantum well defining this lead. In the narrow leads, where the quantum well width is smaller, $d_1 < d_2$, the ground state energy $E_0^{(1)}$ is naturally higher. This energy mismatch is represented by step-like potentials outside the dot region. Inside the quantum dot, electrons can occupy confined states labeled as $E_n^{(D)}$ ($n = 1, 2, \dots$). These are purely quantum confined states with no classical analog: low energy electrons in the dot are confined solely because they do not have enough energy to overcome the narrow channel ground state energy $E_0^{(1)}$.

16 September 2024, 10:10:07

magnitude of usual band offsets between III-V semiconductors,²² and keep $d_2 = 100$ Å and $L = 50$ Å in all calculations.

Notice that, classically, particles in such a potential are not confined in the horizontal direction, x axis, since they are allowed to escape the system through the leads. In quantum mechanics, on the other hand, a charge carrier in the ground state $E_0^{(D)}$ of the quantum dot has lower energy than the ground state $E_0^{(2)}$ of the quantum wells that form the leads, so that the lowest energy state of the whole system in Fig. 1 consists of a quantum confined particle inside the dot region.^{19–21} If one now assumes a constriction in the leads-dot junction, the ground state of the constriction has even higher energy $E_0^{(1)}$. The effective energy profile across the central horizontal axis of the system in Fig. 1(a) is sketched in Fig. 1(b).

As incident light interacts with an electron initially in the ground state of the dot, it excites the electron to higher energy

states, provided the light frequency matches the energy of allowed transition between quantum dot states. In the configuration of dot and leads states illustrated in Fig. 1(b), for example, if the electron is excited from $E_0^{(D)}$ to $E_2^{(D)}$ by light, it is able to tunnel through the constrictions and leave the system through the leads, thus producing a photo-generated current J . This requires the system to be designed in a way where the transition between the ground state of the dot $E_0^{(D)}$ and its target final state (e.g., $E_2^{(D)}$) is allowed by selection rules, but this can be arranged by properly tuning the quantum dot radius and well widths. The effective energy profile in Fig. 1(b) bears a resemblance to the one proposed in Ref. 6, where the profile is created by band offsets between conduction bands of different semiconductors in a heterostructure. The constrictions in our case play the role of the buffer layers as in Ref. 6, which tune the sharpness of photo-current peaks by controlling quantum tunnelling across them. The band mismatch between III–V semiconductors is usually of the order of hundreds of meV, whereas the difference between the quantum dot and quantum well states proposed here is of the order of a few tens of meV. Therefore, the system proposed here can be seen as an analog of the one in Ref. 6 that operates in the terahertz range.

In order to simulate the photo-generated current in the system in Fig. 1, the electron–photon interaction is described by a time-oscillating electric field potential $-eyE_{dyn}\cos(\omega t)$, where E_{dyn} is the amplitude of the electric field (namely, related to light intensity) and ω is its oscillation frequency. A static electric field E_{st} is applied along the channels, i.e., in the x -direction, in order to provide a bias voltage between the leads and, therefore, produce non-zero net current. The Hamiltonian is written within the effective mass approximation,

$$H = -\frac{\hbar^2}{2m^*} \nabla^2 + V(x, y) - eyE_{dyn}\cos(\omega t) - exE_{st}, \quad (1)$$

where m^* is the electron effective mass and $V(x, y)$ is the potential profile depicted in Fig. 1(a). All calculations were performed assuming the effective mass of electrons in GaAs, namely, $m^* = 0.067m_0$, where m_0 is the free electron mass.

The time-dependent Schrödinger equation for this system is solved by the split-operator technique^{17–20,23} in two steps: first, the method is used to evolve an arbitrary initial wave function in imaginary time $\tau = it$ in the absence of light ($E_{dyn} = 0$). This procedure makes the arbitrary wave function converge to the ground state of the system as $\tau \rightarrow \infty$.²³ Second, we assume this ground state wave function as the initial wave function $\psi(\vec{r}, 0)$ for real time propagation; now in the presence of light, i.e., $E_{dyn} \neq 0$. In both cases, time evolution is performed by applying the time evolution operator

$$\psi(\vec{r}, t + \Delta t) = \exp\left(-\frac{i}{\hbar} \int_t^{t+\Delta t} H(t') dt'\right) \psi(\vec{r}, t) \quad (2)$$

to propagate a wave function at time t to $t + \Delta t$. Since the potential $V_t = V(x, y) - eyE_{dyn}\cos(\omega t) - exE_{st}$ and kinetic T energy operators do not commute, the time evolution operator in Eq. (2) is split

and approximated as

$$e^{-i \int_t^{t+\Delta t} \frac{V_t + V_t}{\hbar} dt} = e^{-i \int_t^{t+\Delta t} \frac{V_t}{\hbar} dt} e^{-i \frac{\Delta t}{\hbar} E_{st}} e^{-i \int_t^{t+\Delta t} \frac{V_t}{\hbar} dt} + O(\Delta t^3), \quad (3)$$

where the $O(\Delta t^3)$ error is made negligible by assuming small time steps Δt . The integral appears because of time dependence of the potential in time due to light. It can be calculated using the V_t definition,

$$\int_t^{t+\Delta t} V_t(t') dt' = (V - exE_{st})\Delta t - \frac{2eyE_{dyn}}{\omega} \cos\left[\frac{2\omega t + \omega\Delta t}{2}\right] \sin\left[\frac{\omega\Delta t}{2}\right]. \quad (4)$$

Since kinetic energy operators for different directions commute, their exponentials can be separated exactly. Each exponential is, thus, expanded in the Cayley²⁴ form and applied through a matrix method, as described in Ref. 23.

Applying these operators successively, one evolves the initial wave function from $t = 0$ to any $t > 0$. In the case of real time propagation, light induced scattering processes between the ground state and the excited ones that are not forbidden by selection rules are naturally obtained by such numerical procedure.

Probability density currents outward the leads of width d_2 in Fig. 1(a) are calculated using

$$\vec{J}(x_p, t) = \frac{\hbar}{m} \int_{-\infty}^{\infty} \Im \left[\psi^* \frac{\partial \psi}{\partial x} \right]_{x_p} dy, \quad (5)$$

where $P = L$ (R) refers to left (right) leads, respectively, and the derivative is numerically performed with a finite difference scheme. The photo-current in a given lead P is obtained as the current in that lead integrated in time,

$$J = \int_0^{T_{\max}} \vec{J}(x_p, t) dt, \quad (6)$$

where the maximum time of simulation T_{\max} can be interpreted as a response time of the photo-current system proposed here. In the absence of static fields ($E_{st} = 0$), we consider the photo-current only in one of the leads.²⁵ For $E_{st} \neq 0$, the net photo-current is defined as the difference between integrated currents in the left and right leads. A 5000 Å long computational box is considered in the x direction, currents are computed at $x_R = -x_L = 1590$ Å, and we fix the maximum time at $T_{\max} = 3000$ fs in all calculations. Notice that for a long simulation time, Rabi oscillations would play an important role, with the wavefunction periodically populating the excited states $E_1^{(D)}, E_2^{(D)}, \dots$ of the quantum dot and, consequently, periodically tunneling out of it through the leads. Nevertheless, we have checked that, for the parameters used in this work, such $T_{\max} = 3000$ fs simulation time does not cover several periods of the Rabi oscillations; therefore, they do not lead to significant effects in our results.

Once the propagated wave function reaches the boundaries of the computational box, it is expected to get a spurious reflection.

Of course, this reflection has no physical meaning and is just an artifact of the numerical procedure taken here. In order to avoid it, our numerical model uses an absorption region,²⁶ based on a smooth imaginary potential, which makes the wave function vanish before it actually reaches the boundaries of the computational grid.

III. RESULTS AND DISCUSSION

Let us first provide a proof-of-concept discussion on the effect of constrictions on the transmission probabilities in the quantum dot system sketched in Fig. 1(a). We initially focus on the zero bias case ($E_{st} = 0$) and discuss the effect of a finite bias later on. Transmission probabilities calculated using the scattering matrix approach of the Kwant package²⁷ are shown in Fig. 2, assuming a quantum dot radius $R = 110 \text{ \AA}$ and three different values for constrictions width d_1 . This represents the probability for an electron to cross the quantum dot system from its left lead to the right one. Electrons with energy lower than $\approx 50 \text{ meV}$, even if they have enough energy to populate the ground state of the quantum wells forming the leads (namely, 39 meV for the parameters chosen here), are unable to cross the quantum dot, unless the electron energy matches a quantum state of the dot. The ground state of the quantum dot has energy lower than that of the leads, but the first and second excited states of the dot, represented by the vertical green dotted lines in Fig. 2, have enough energy to allow for quantum transport across the system. This explains why transmission probability for $d_1 = d_2$ (blue dotted) is almost one for any energy above $E_1^{(D)}$. In fact, the high transmission probability starts from an energy slightly lower than $E_1^{(D)}$, because opening the channels effectively slightly reduces the energy of quantum dot states.

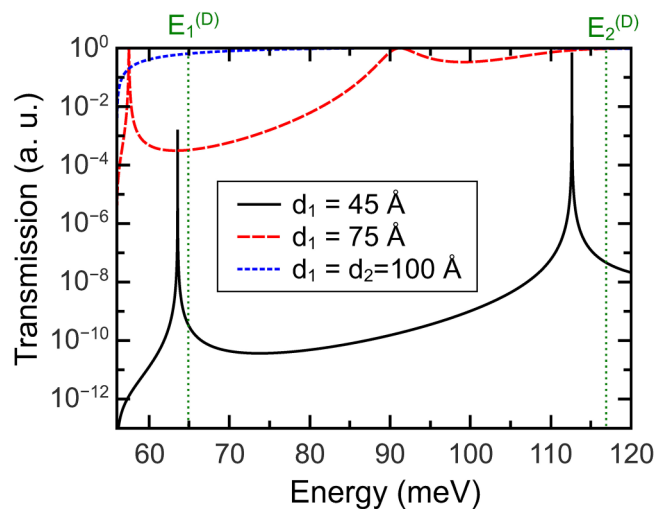


FIG. 2. Transmission probabilities across the system in Fig. 1(a), assuming a quantum dot radius $R = 110 \text{ \AA}$, leads with width $d_2 = 100 \text{ \AA}$ and constrictions with length $L = 50 \text{ \AA}$ and width $d_1 = 100 \text{ \AA}$ (blue dotted), 75 \AA (red dashed), and 45 \AA (black solid). Vertical green lines mark the energies of the first $E_1^{(D)}$ and second excited $E_2^{(D)}$ states of an isolated quantum dot with the same radius and effective mass.

If one now considers a constriction, $d_1 < d_2$ (red dashed and black solid lines), very narrow peaks appear at energies that get closer to $E_1^{(D)}$ and $E_2^{(D)}$ as d_1 decreases. This supports the idea that the narrow constrictions effectively act as high energy barriers, as depicted in Fig. 1(b), so that the narrow peaks now are reminiscent of the quantum resonant tunneling effect in a double barrier system.²⁸ As we will show in what follows, the same effect is observed for photo-generated currents in this system, where the constrictions sharpen photo-current peaks originating from light induced transitions from $E_0^{(D)}$ to $E_n^{(D)}$ states.

Notice that the state labeled by $E_1^{(D)}$ is actually doubly degenerate, with wave functions exhibiting p_x and p_y symmetries. The narrow channels attached to the dot break the circular symmetry, thus slightly lifting this degeneracy and effectively creating two new energy states $E_{1,x}^{(D)}$ and $E_{1,y}^{(D)}$. Even so, only one peak is actually observed in Fig. 2. This is due to the fact that the wavefunction of the resonant $E_{1,y}^{(D)}$ has a nodal line at $y = 0$, inhibiting thereby tunneling through it from the y -symmetric incoming state in the lead. The same reasoning applies to the two D-like states related to $E_2^{(D)}$.

Figure 3 shows the photo-current spectrum of the proposed device as a function of energy $\hbar\omega$ of the incident light. For $d_1 = d_2 = 100 \text{ \AA}$, i.e., in the absence of constrictions, Fig. 3(a) shows non-zero photo-current for a wide range of energies around a few tens of meV, namely, for incident light with energy enough to induce $E_0^{(D)}$ to $E_{1,y}^{(D)}$ transition. For the radii considered here, this excited state has enough energy to leave the quantum dot through the leads. As the constriction is made narrower, see Fig. 3(b) for $d_1 = 75 \text{ \AA}$, the photo-current peaks become sharper, until two peaks are clearly observed in Fig. 3(c) for $d_1 = 45 \text{ \AA}$, both with energies lying in the range of a few tens of meV, i.e., with terahertz frequencies. The higher energy peak exhibits lower current maximum.

Let us take a closer look in these sharp peaks for $d_1 = 45 \text{ \AA}$ in Fig. 3(c). Their energies are predicted by the difference between the energies of confined states of the quantum dot, as shown in Fig. 4. As the radius increases, the energy of the peaks decreases (solid curves). The first (lowest energy) peak clearly follows the radius-dependent energy gap $E_{1,y}^{(D)} - E_0^{(D)}$ between the ground and first excited states of the quantum dot, which confirms the $E_0^{(D)}$ to $E_{1,y}^{(D)}$ transition as its origin. The second peak, however, does not match the transition energy between any pair of states. Instead, it matches very well $(E_3^{(D)} - E_0^{(D)})/2$, which points toward the possibility of a second-order absorption process. The latter is zero-angular-momentum ($l = 0$) state of the isolated circular QD, which has a node in the wave function along the radial direction, i.e., a $2s$ -like state. Notice that the light polarized along Oy does not directly couple the ground $1s$ -like and this excited $2s$ -like state, but since we are not using perturbative methods, transitions between them may appear. It is important to provide strong arguments to ensure that the higher energy peak observed in Figs. 3 and 4 does indeed come from a second-order phenomenon.

This is clearly demonstrated in Fig. 5, which shows the maximum photo-current of each peak as a function of the amplitude of the dynamic electric field. The lowest order photocurrent is expected to vary linearly with light intensity (thus, quadratically with E_{dyn}). This is indeed observed for the lowest energy photocurrent peak, represented by solid symbols in Fig. 5, which agrees well

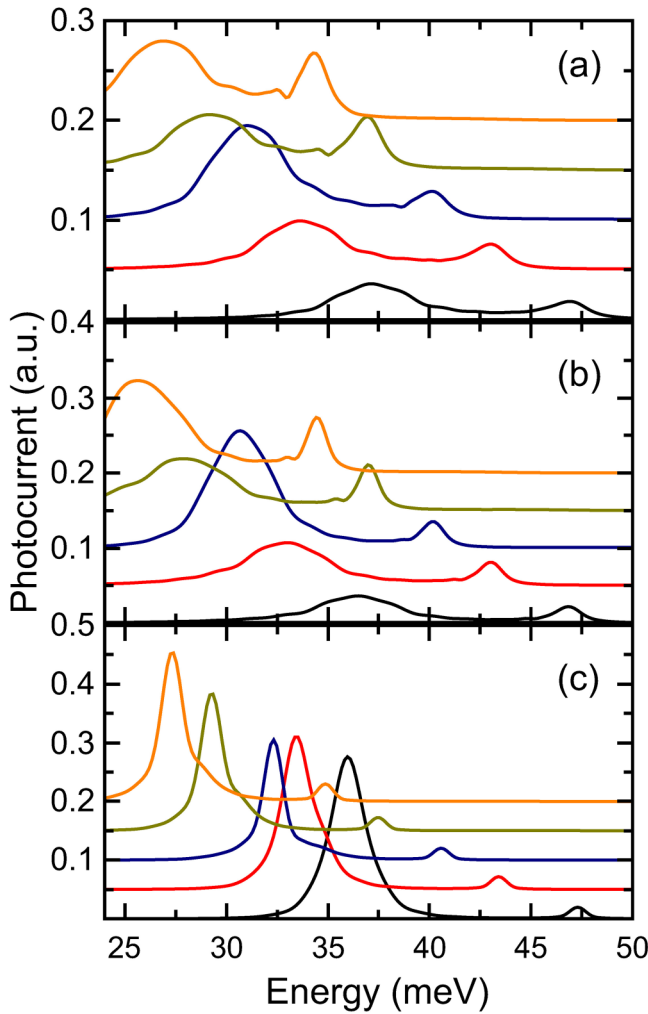


FIG. 3. Calculated photocurrent in the leads as a function of energy $\hbar\omega$ of the incident light, assuming $E_{dyn} = 5$ kV/cm and different constriction widths (a) $d_1 = d_2 = 100$ Å (i.e., no constriction), (b) $d_1 = 75$ Å, and (c) $d_1 = 45$ Å. Results for quantum dots with radii $R = 110$ Å, 115 Å, 120 Å, 125 Å, and 130 Å are shown by curves with different colors, respectively, from lower (black) to higher (orange). The curves were hardshifted by 0.1 from each other in order to improve visualization.

with $J_{max} = \alpha E_{dyn}^2$ (solid lines) for $d_1 = 45$ Å (black circles) and $d_1 = 75$ Å (red triangles), with $\alpha = 9 \times 10^{-3}$ and $\alpha = 3 \times 10^{-3}$, respectively. The slight discrepancy between the quadratic fit and the numerical results in the top two curves and symbols in Fig. 5 is explained by the fact that other higher order transitions also take place at this frequency, as we will discuss in further detail later on. The second peak, however, exhibits a quite different dependence on the electric field, which can be properly fitted to a fourth-order function of the field, just as expected for a second-order effect in a time-dependent perturbation theory. This can be seen in the bottom two curves and symbols in Fig. 5, where the maximum

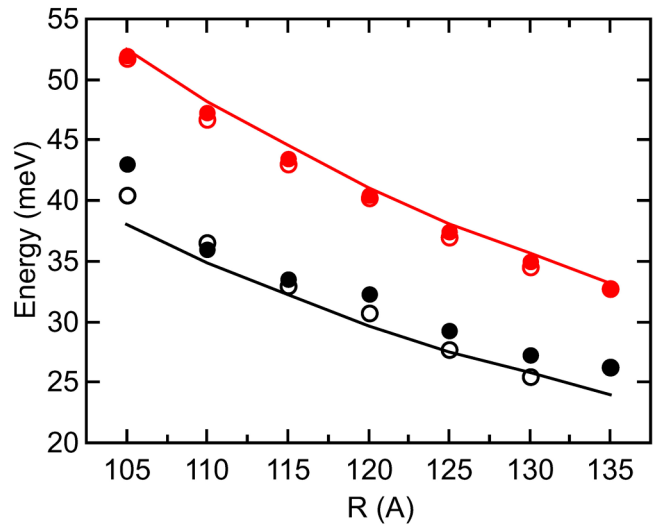


FIG. 4. Energy of the peaks observed in Fig. 3 as a function of the quantum dot radius, assuming $E_{dyn} = 5$ kV/cm. Full (open) symbols are numerical results for the dot-leads system assuming $d_1 = 45(75)$ Å, whereas lines are analytical results for the difference between the ground state and excited state energies of the isolated dot. Lower energy peaks (black symbols) are consistent with $E_0^{(D)}$ to $E_{1,y}^{(D)}$ transition, with energy $E_{1,y}^{(D)} - E_0^{(D)}$ (black line). Higher energy peaks (red symbols) are consistent with a second-order process between $E_0^{(D)}$ and $E_3^{(D)}$, with energy $(E_0^{(D)} - E_3^{(D)})/2$ (red line).

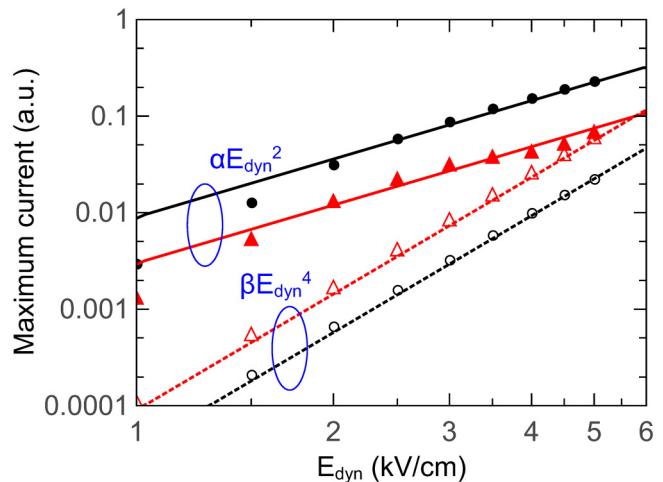


FIG. 5. Maximum value of the photo-generated current peaks in a $R = 125$ Å, $d_1 = 45$ Å (black dots), and $d_1 = 75$ Å (red triangles) system as a function of the electric field amplitude. Full (open) symbols refer to the low (high) frequency current peaks observed in Fig. 3, which fit well to a second (fourth) order function, as shown by the solid (dashed) line.

16 September 2024 10:10:07

current in the higher energy peaks, represented by open symbols, is well fitted to $I_{\max} = \beta E_{\text{dyn}}^4$ for $d_1 = 45 \text{ \AA}$ (black circles) and $d_1 = 75 \text{ \AA}$ (red triangles) with $\beta = 9 \times 10^{-5}$ and $\beta = 3.6 \times 10^{-5}$, respectively. It is important to point out that the results both in Figs. 3 and 5 were obtained with a fixed simulation time T_{\max} , which, as previously discussed, would play the role of a response time of the system under investigation. Different values of T_{\max} would lead to different values of maximum current. Nevertheless, results are qualitatively the same and the conclusions drawn from Fig. 5 still hold provided the simulation time T_{\max} is not long enough to cover many periods of Rabi oscillations between the quantum dot states, as is the case in the results shown here.

Second-order perturbation theory for an oscillating electric field with frequency ω leads to transition rates between $E_0^{(D)}$ and $E_n^{(D)}$ states, with eigenfunctions $|0\rangle$ and $|n\rangle$, respectively, as

$$R_{0 \rightarrow n}^{(2)} = \frac{2\pi e^4 E_{\text{dyn}}^4}{\hbar^4} \left| \sum_m \frac{\langle n|y|m\rangle \langle m|y|0\rangle}{\omega_{m0} - \omega - i\epsilon} \right|^2 \delta(\omega_{n0} - 2\omega), \quad (7)$$

where $\hbar\omega_{m0} = \hbar\omega_m - \hbar\omega_0 = E_m^{(D)} - E_0^{(D)}$. The fourth-order dependence of the transition rates on E_{dyn} is obvious from Eq. (7), thus agreeing well with the field dependence observed for the maximum current in the higher energy peak (open symbols) in Fig. 5. The δ -function in Eq. (7) suggests that light needs half the energy $E_n^{(D)} - E_0^{(D)}$ to be able to induce a second-order transition from $|0\rangle$ and $|n\rangle$, which can be also interpreted as being due to a two-photon absorption by the electron system. This explains the halved $E_3^{(D)} - E_0^{(D)}$ energy used to match the higher energy peaks in Fig. 3. Similar multiple-photon analysis has been made in the context of quantum wells and dots in Refs. 6, 29, and 30, where such non-linear processes are also observed. Finally, one has to check which virtual transitions are allowed by selection rules in Eq. (7) in order to verify the possibility of a second-order light-mediated transition between $E_0^{(D)}$ and $E_3^{(D)}$, as suggested in Fig. 3.

Indeed, Eq. (7) straightforwardly explains the calculated second-order dependencies of square intensity (forth power of E_{dyn}) and energy position of the resonance at half-way between the ground state and an excited one of the dot not directly coupled to it by dipolar coupling. Let us for simplicity assume the states of an isolated dot and infinite confinement ($V_0 = \infty$). For $R = 125 \text{ \AA}$, we obtain the energies 18, 45.5, 81.1, and 94.1 meV for the $|1S\rangle$, $|1P_{x,y}\rangle$, $|1D_{x,y}\rangle$, and $|2S\rangle$ states, respectively. Light directly couples the ground $|1S\rangle$ to the $|1P_y\rangle$ state (resonance around 27.5 meV), whereas the later serves as an intermediate state to a subsequent excitation toward either the $|1D_y\rangle$ or $|2S\rangle$ states, with energy resonances for such second-order processes around 31.5 and 38 meV. Both the linear peak and the non-linear one involving $|2S\rangle$ fit very well with the results in Figs. 3 and 4, with small discrepancies mostly related to the influence of the leads on the dot states. The absence of $1D_y$ -related second-order peak is due to its much smaller matrix element and the fact that the transition energy for this case would be similar to the one of the lowest energy peaks (both being at ≈ 30 meV), thus being masked by it. In fact, that is consistent with the asymmetry observed in the low energy peaks in Fig. 4, which are possibly made by a composition of two peaks with slightly different energies.

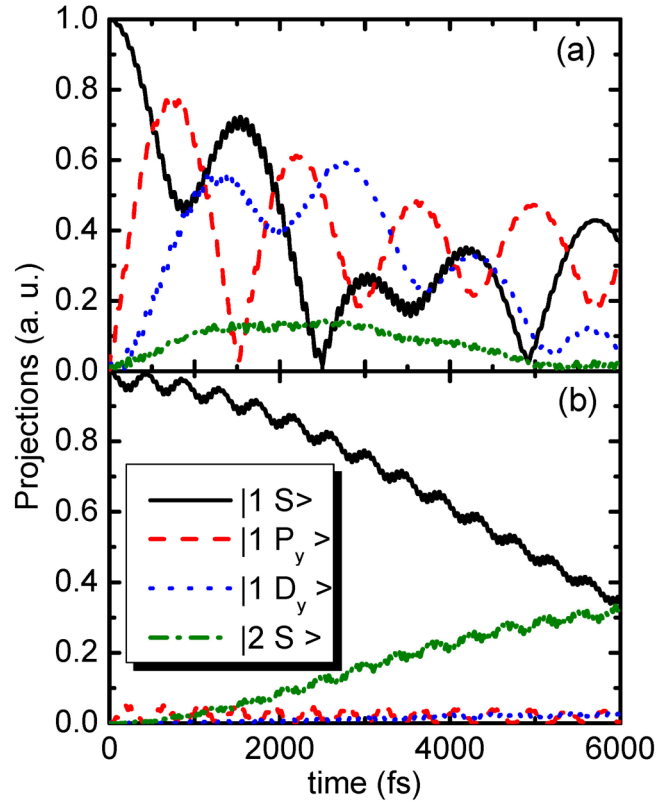


FIG. 6. Time evolution of the projections of the propagated wave function onto the relevant eigenstates of a circular quantum dot ($|1S\rangle$, $|1P_y\rangle$, $|1D_y\rangle$, and $|2S\rangle$) for a $R = 125 \text{ \AA}$ and $d_1 = 45 \text{ \AA}$ system under a field with $E_{\text{dyn}} = 5 \text{ kV/cm}$ and frequencies (a) $\omega = 29.25 \text{ meV/h}$ (lowest energy peak in Fig. 4) and (b) 37.5 meV/h (highest energy peak in Fig. 4). Projections onto other eigenstates such as $|1P_x\rangle$ and $|1D_x\rangle$ are negligibly small due to selection rules.

16 September 2024, 10:10:07

The participation of higher order transitions in the time evolution investigated here is further confirmed by the time dependence of the projections of the propagated wave function onto the eigenstates of a circular quantum dot, $\langle \psi | n \rangle$ ($n = 1S, 1P_{x,y}, 1D_{x,y}$, or $2S$). As an example, Fig. 6 shows the results for a $R = 125 \text{ \AA}$ and $d_1 = 45 \text{ \AA}$ system under an electric field with $E_{\text{dyn}} = 5 \text{ kV/cm}$. Notice that in this figure, the simulation time is exceptionally longer as compared to $T_{\max} = 3000 \text{ fs}$ assumed in the other figures in order to illustrate better the interplay between different quantum dot states as time evolves. Two frequencies of the dynamical field are considered: (a) $\omega = 29.25 \text{ meV/h}$, corresponding to the lowest energy peak in Fig. 4 and (b) 37.5 meV/h that corresponds to the highest energy peak in Fig. 4. These results reveal that the only states involved in the time evolution of the wave packet are the aforementioned ones, whereas projections onto other eigenstates of the quantum dot, such as $|1P_x\rangle$ and $|1D_x\rangle$, are negligibly small, due to the previously discussed selection rules. The peak at $\omega = 29.25 \text{ meV/h}$ for this system clearly involves not only the first order $|1S\rangle - |1P_y\rangle$ transition, but also higher order intermediate

transitions to $|1D_y\rangle$ and $|2S\rangle$ states, which explains why the numerical results do not perfectly fit the quadratic behavior that is expected from the first-order time-dependent perturbation theory in Fig. 5. For the higher energy peak, on the other hand, Fig. 6(b) shows much weaker projections onto the intermediate $|1P_y\rangle$ and $|1D_y\rangle$ states, while the projection onto $|2S\rangle$ is clearly stronger. As a consequence, the fourth-order fitting for such higher energy peak in Fig. 5 exhibits better agreement with the numerical results.

It is also worth stressing that the appearance of non-linear features for light fields of a few kV/cm is due to the large dot size: indeed, for a 200 Å diameter the potential drop inside the dot is 10 meV for $E_{dyn} = 5$ kV/cm, which is a sizeable fraction of typical energy spacing between the dot states. Note finally that for the dot radii considered here both the linear and non-linear photo-response peaks are in the same spectral range, i.e., in the THz domain.

With the physical nature of low and high frequency peaks in Fig. 3 fully understood, we now investigate how a non-zero static field E_{st} can be used to control the net current in each of these frequencies. This is shown in Figs. 7(a) and 7(b) for the high and low

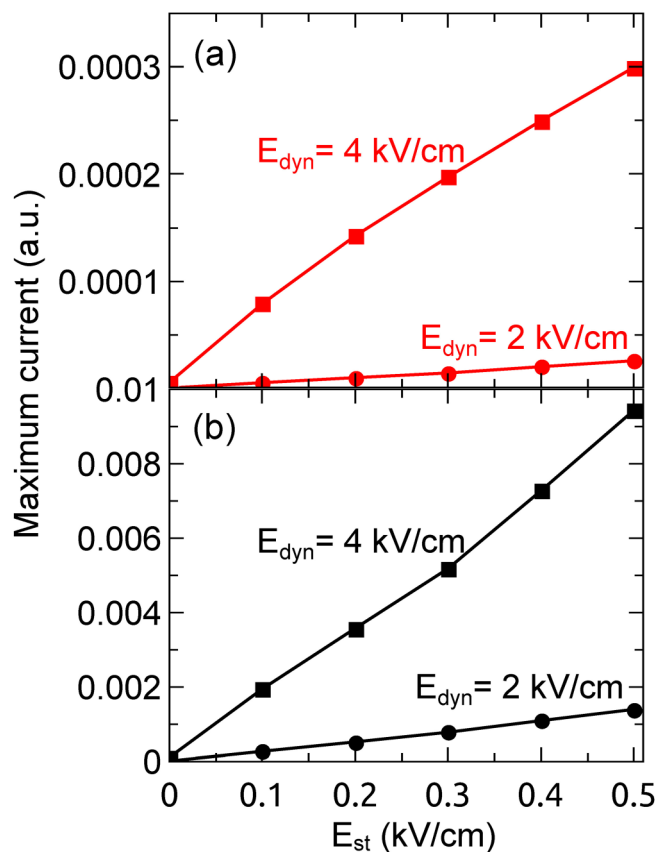


FIG. 7. Maximum net current in the (a) higher and (b) lower frequency peaks in Fig. 3(c), for $R = 125$ Å and $d_1 = 45$ Å, as a function of static electric field E_{st} . Two values of the dynamic electric field are considered, $E_{dyn} = 2$ (circles) and 4 kV/cm (squares).

frequency peaks of a $R = 125$ Å and $d_1 = 45$ Å system, respectively. The results show that the net current increases with the static field, and that the dependence is significantly stronger when the dynamical field is higher. Note, in particular, that in the weak bias case considered here (the energy difference between the left and right leads due to the bias is at most 1.75 meV for $E_{st} = 0.5$ kV/cm), the net current is apparently linear with the applied voltage for weak E_{dyn} but becomes slightly non-linear at higher E_{dyn} . The high frequency peak is also shown to be less susceptible to the static field, with a much lower increase between $E_{st} = 0$ and $E_{st} = 0.5$ kV/cm in Fig. 7(a), results for the low frequency peak in Fig. 7(b).

IV. CONCLUSIONS

In summary, we have calculated the photo-generated current in a semiconductor quantum dot attached to leads. Under light excitation, a photo-generated current in this device is peaked at very low frequencies, thus suggesting this system as a candidate for a photo-current device operating with THz frequencies. Using a narrow constriction between the leads and the dot, one can control the width of the photo-current peak, whereas the radius of the dot can be used to tune the peak frequency.

An extra higher energy peak is observed and identified as being due to a second-order transition, i.e., a transition that can be only captured by a second-order correction using the time-dependent perturbation theory. This is verified (i) by the fact that the height of this peak depends on the electric field intensity to the power of four, in contrast to the usual dependence on the squared electric field, as expected for first-order transitions, and (ii) by actually calculating the time evolution of the projections of the propagated wave function onto the eigenstates of a quantum dot, where the interplay between four different eigenstates can be observed.

Although the system proposed here, for the sake of simplicity, has been investigated without taking into account temperature effects, disorder, electron–electron interactions, and other possible scattering mechanisms, we believe the proof-of-concept proposed here can stimulate more future studies toward realization of photo-current nanodevices and related technologies operating in THz frequencies.

ACKNOWLEDGMENTS

Discussions with TAS Pereira and AA Sousa are gratefully acknowledged. This work was supported by the Brazilian Council for Research (CNPq) through the PRONEX/FUNCAP and PQ programs.

DATA AVAILABILITY

The data that support the findings of this study are available from the corresponding author upon reasonable request.

REFERENCES

- R. H. Hadfield, *Nat. Photonics* **3**, 696 (2009).
- H. C. Liu, M. Gao, J. McCaffrey, Z. R. Wasilewski, and S. Fafard, *Appl. Phys. Lett.* **78**, 79 (2001).

16 September 2024, 10:10:07

- ³X. Wang, Z. Cheng, K. Xu, H. K. Tsang, and J. Xu, *Nat. Photonics* **7**, 888–891 (2013).
- ⁴H. Pettersson, J. Trägårdh, A. I. Persson, L. Landin, D. Hessman, and L. Samuelson, *Nano Lett.* **6**, 229 (2006).
- ⁵S. Keuleyan, E. Lhuillier, V. Brajuskovic, and P. Guyot-Sionnest, *Nat. Photonics* **5**, 489–493 (2011).
- ⁶M. H. Degani, M. Z. Maialle, P. F. Farinas, and N. Studart, *J. Appl. Phys.* **110**, 104313 (2011).
- ⁷J. Federici and L. Moeller, *J. Appl. Phys.* **107**, 111101 (2010).
- ⁸T. Kleine-Ostmann and T. Nagatsuma, *J. Infrared Milli. Terhz. Waves* **32**, 143–171 (2011).
- ⁹T. Nagatsuma, S. Horiguchi, Y. Minamikata, Y. Yoshimizu, S. Hisatake, S. Kuwano, N. Yoshimoto, J. Terada, and H. Takahashi, *Opt. Express* **21**, 23736 (2013).
- ¹⁰A. D. Stiff-Roberts, *J. Nanophotonics* **3**, 031607 (2009).
- ¹¹C. Livache, B. Martinez, N. Goubet, C. Gréboval, J. Qu, A. Chu, S. Royer, S. Ithurria, M. G. Silly, B. Dubertret, and E. Lhuillier, *Nat. Commun.* **10**, 2125 (2019).
- ¹²X. H. Su, J. Yang, and P. Bhattachary, *Appl. Phys. Lett.* **89**, 031117 (2006).
- ¹³W. Wu, D. Dey, and H. Mohseni, *J. Phys. D Appl. Phys.* **43**, 155101 (2010).
- ¹⁴Y. Zhang, K. Shibata, N. Nagai, C. Ndebeka-Bandou, G. Bastard, and K. Hirakawa, *Nano Lett.* **15**, 1166 (2015).
- ¹⁵D. N. Basov, M. M. Fogler, and F. J. García de Abajo, *Science* **354**, aag1992 (2016).
- ¹⁶T. Low, A. Chaves, J. D. Caldwell, A. Kumar, N. X. Fang, P. Avouris, T. F. Heinz, F. Guinea, L. Martin-Moreno, and F. Koppens, *Nat. Mater.* **16**, 182 (2017).
- ¹⁷A. A. Sousa, A. Chaves, G. A. Farias, and F. M. Peeters, *Phys. Rev. B* **88**, 245417 (2013).
- ¹⁸A. A. Sousa, A. Chaves, T. A. S. Pereira, G. A. Farias, and F. M. Peeters, *Physica E* **114**, 113598 (2019).
- ¹⁹M. H. Degani, *Phys. Rev. B* **66**, 233306 (2002).
- ²⁰F. Batista, A. Chaves, D. R. da Costa, and G. Farias, *Physica E* **99**, 304–309 (2018).
- ²¹R. L. Schult, D. G. Ravenhall, and H. W. Wyld, *Phys. Rev. B.* **39**, 5476 (1988).
- ²²A. Chaves, G. A. Farias, F. M. Peeters, and B. Szafran, *Phys. Rev. B* **80**, 125331 (2009).
- ²³A. Chaves, G. A. Farias, F. M. Peeters, and R. Ferreira, *Commun. Comput. Phys.* **17**, 850–866 (2015).
- ²⁴N. Watanabe and M. Tsukada, *Prog. Theor. Phys. Suppl.* **138**, 115–116 (2000).
- ²⁵In this case, the current can be calculated either in the left or in the right lead, leading to equivalent results, due to symmetry.
- ²⁶R. Kosloff and D. Kosloff, *J. Comput. Phys.* **63**, 363–376 (1986).
- ²⁷C. W. Groth, M. Wimmer, A. R. Akhmerov, and X. Waintal, *New J. Phys.* **16**, 063065 (2014).
- ²⁸L. L. Chang, L. Esaki, and R. Tsu, *Appl. Phys. Lett.* **24**, 593 (1974).
- ²⁹D. R. Alvarenga, C. A. Parra-Murillo, R. M. S. Kawabata, P. S. S. Guimaraes, K. Unterrainer, M. P. Pires, G. S. Vieira, J. M. Villas-Boas, M. Z. Maialle, M. H. Degani, P. F. Farinas, N. Studart, and P. L. Souza, *IEEE J. Quantum Electron.* **48**, 1360 (2012).
- ³⁰M. H. Degani, M. Z. Maialle, P. F. Farinas, N. Studart, M. P. Pires, and P. L. Souza, *J. Appl. Phys.* **109**, 064510 (2011).